

DOI: 10.1002/ ((please add manuscript number))

Article type: Full paper

# Improved Optics in Monolithic Perovskite/Silicon Tandem Solar Cells with a Nanocrystalline Silicon Recombination Junction

*Florent Sahli\*,<sup>1</sup> Brett A. Kamino,<sup>2</sup> Jérémie Werner,<sup>1</sup> Matthias Bräuninger,<sup>1</sup> Bertrand Paviet-Salomon,<sup>2</sup> Loris Barraud,<sup>2</sup> Raphaël Monnard,<sup>1</sup> Johannes Peter Seif,<sup>1</sup> Andrea Tomasi,<sup>1</sup> Quentin Jeangros,<sup>1,3</sup> Aïcha Hessler-Wyser,<sup>1</sup> Stefaan De Wolf,<sup>1,a</sup> Matthieu Despeisse,<sup>2</sup> Sylvain Nicolay,<sup>2</sup> Bjoern Niesen\*,<sup>1,2</sup> and Christophe Ballif<sup>1,2</sup>*

F. Sahli, Dr. B. A. Kamino, J. Werner, Dr. M. Bräuninger, Dr. B. Paviet-Salomon, L. Barraud, R. Monnard, Dr. J. P. Seif, Dr. A. Tomasi, Dr. Q. Jeangros, Dr. A. Hessler-Wyser, Prof. S. De Wolf, Dr. M. Despeisse, Dr. S. Nicolay, Dr. B. Niesen, Prof. C. Ballif

<sup>1</sup> Ecole Polytechnique Fédérale de Lausanne (EPFL), Institute of Microengineering (IMT) Photovoltaics and Thin-Film Electronics Laboratory (PV-Lab), Rue de la Maladière 71b, 2002 Neuchâtel, Switzerland.

<sup>2</sup> CSEM, PV-Center, Jaquet-Droz 1, 2002 Neuchâtel, Switzerland.

<sup>3</sup> University of Basel, Department of Physics, Klingelbergstrasse 82, CH-4056 Basel, Switzerland.

E-mail: [florent.sahli@epfl.ch](mailto:florent.sahli@epfl.ch), [bjoern.niesen@csem.ch](mailto:bjoern.niesen@csem.ch)

Keywords: microcrystalline, organic-inorganic perovskite, multijunction, tunnel junction, silicon heterojunction.

---

<sup>a</sup> Now at King Abdullah University of Science and Technology (KAUST), KAUST Solar Center (KSC), Thuwal 23955-6900, Saudi Arabia

**Abstract**

Perovskite/silicon tandem solar cells are increasingly recognized as promising candidates for next-generation photovoltaics with performance beyond the single-junction limit at potentially low production costs. Current designs for monolithic tandems rely on transparent conductive oxides as an intermediate recombination layer, which lead to optical losses and reduced shunt resistance. We demonstrate an improved recombination junction based on nanocrystalline silicon layers to mitigate these losses. When employed in monolithic perovskite/silicon heterojunction tandem cells with a planar front side, this junction is found to increase the bottom cell photocurrent by more than 1 mA/cm<sup>2</sup>. In combination with a cesium-based perovskite top cell, this leads to tandem cell power-conversion efficiencies of up to 22.7% obtained from *J-V* measurements and steady-state efficiencies of up to 22.0% during maximum power point tracking. Thanks to its low lateral conductivity, the nanocrystalline silicon recombination junction enables upscaling of monolithic perovskite/silicon heterojunction tandem cells, resulting in a 12.96 cm<sup>2</sup> monolithic tandem cell with a steady-state efficiency of 18%.

## 1. Introduction

As the cost of photovoltaic (PV) modules has fallen steeply to currently less than 50% of that of the overall PV system, enhancing solar cell performance represents the most effective way to further reduce the cost of PV electricity.<sup>[1][2]</sup> The most viable approach to reach efficiencies well beyond those of today's commercial solar cell technologies, such as crystalline silicon (c-Si), is to form a tandem device by combining a narrow-bandgap bottom cell with a top cell exhibiting a wider bandgap, thereby reducing thermalization losses.

Recently, organic-inorganic lead halide perovskite solar cells were identified as promising wide-bandgap top cell candidates due to their high power output efficiencies,<sup>[3][4]</sup> sharp optical absorption edge,<sup>[5]</sup> and tunable bandgap, which can match the optimal value of 1.7-1.8 eV for tandems with a c-Si bottom cell.<sup>[6]</sup> Thanks to these properties, perovskite/c-Si tandem cells have an efficiency potential well above 30% with low-cost manufacturing.<sup>[7][8]</sup> So far, perovskites have successfully been employed in tandem cells with bottom cells based on c-Si, chalcogenides, and narrow-bandgap perovskites.<sup>[9][10][11][12][13]</sup> Silicon heterojunction (SHJ) bottom cells enabled the highest efficiencies reported for perovskite-based tandems due to their high open-circuit voltage,<sup>[14]</sup> excellent near-infrared response<sup>[15]</sup> and power conversion efficiencies above 26%.<sup>[16]</sup>

Among the different possible tandem configurations, including 4-terminal mechanically stacked cells<sup>[17][18]</sup> and devices using a spectral splitter,<sup>[19]</sup> the monolithically integrated 2-terminal tandem configuration, in which the top cell is directly deposited onto the bottom cell, arguably has the highest potential to reach a low levelized cost of electricity (LCOE). Nevertheless, monolithic sub-cell integration requires top cell processing conditions that are compatible with the underlying bottom cell, which makes manufacturing more challenging than for mechanically-stacked tandem cells. Furthermore, the overall current of a series-connected 2-terminal tandem is limited to the cell generating the smaller current, requiring appropriate light management to reach high performance.

A crucial element of any 2-terminal tandem cell is the intermediate recombination or tunnel junction connecting both sub-cells in series, ideally enabling collected carriers from one sub-cell to recombine with collected carriers of opposite charge from the other sub-cell without introducing electrical or optical losses. So far, mainly transparent conductive oxides (TCOs) have been used as recombination layers in the fabrication of monolithic perovskite-based tandems.<sup>[11][9][20][21][10]</sup> While in principle effective, this approach suffers from several drawbacks: parasitic absorption of wavelengths above 800 nm due to free-carrier absorption,<sup>[22]</sup> poor refractive index matching with silicon causing enhanced reflection losses at the TCO/silicon interface,<sup>[23]</sup> and high lateral conductivity, promoting shunt paths through the top cell.<sup>[24][25]</sup>

A strategy to effectively mitigate TCO-related optical losses is the integration of a p/n recombination junction as widely used in III-IV semiconductor and thin-film silicon tandem solar cells.<sup>[26][27][28]</sup> A first demonstration of a silicon-based recombination junction for perovskite/silicon tandem cells was made by Mailoa *et al.*, on a diffused-junction c-Si solar cell, although with a limited efficiency of 13.7% and requiring a high-temperature annealing step that is not compatible with SHJ cells.<sup>[29]</sup> A particularly interesting low-temperature (< 200°C) approach lies in using hydrogenated nanocrystalline silicon (nc-Si:H), deposited by plasma-enhanced chemical vapor deposition (PECVD) employing silane gas with high hydrogen dilution.<sup>[27][30]</sup> By adding either trimethylboron or phosphine to the silane/hydrogen mixture in the reactor, highly doped nc-Si:H can be obtained,<sup>[31]</sup> which is required for recombination junctions exhibiting low resistance and narrow-potential energy barrier widths. Such nc-Si:H layers have recently been used for high-efficiency SHJ solar cells in the both-sides-contacted and back-contacted configurations.<sup>[32][33][34]</sup>

This work presents an nc-Si:H recombination junction for monolithic perovskite/silicon heterojunction tandem cells, which reduces reflection and parasitic absorption losses in comparison to a commonly used TCO recombination layer. Using this recombination junction,

we achieved tandem cell efficiencies of up to 22.7% obtained from  $J$ - $V$  measurements and up to 22.0% steady-state efficiencies from maximum power point tracking for an aperture area of 0.25 cm<sup>2</sup>. Thanks to the high device shunt resistance as a result of its low lateral conductivity, this recombination junction enabled tandem cell up-scaling, leading to > 12 cm<sup>2</sup> monolithic perovskite/silicon heterojunction tandems with steady-state efficiencies up to 18%.

## 2. Results and discussions

Monolithic perovskite/SHJ tandem cells with nc-Si:H recombination junctions were fabricated with a layer stack as shown in **Figure 1a**. A rear-side textured SHJ bottom cell in the rear-emitter configuration (i.e., with the hole-collecting side facing sunwards) was used.<sup>[17]</sup> More information regarding device fabrication is given in the Experimental Section. On top of the polished front side of the bottom cell, the p<sup>+</sup>/n<sup>+</sup> nc-Si:H recombination layer stack with a crystallinity of 17.7% ± 0.15, as obtained from Raman spectroscopy (see **Figure S1**), was deposited by PECVD. High-resolution transmission electron microscopy (HRTEM) micrographs of the recombination junction shown in Figure 1c confirm the presence of crystal grains in the nc-Si:H layers. Furthermore, colored inverse fast Fourier transforms (iFFT) generated from several Si (111) and (022) crystalline orientations demonstrate the presence of epitaxial growth between the p- and n-doped regions of the recombination junction, evidenced by crystals spanning across the nc-Si:H(p<sup>+</sup>)/nc-Si:H(n<sup>+</sup>) interface. The position of this interface is inferred from the EDX map (see Figure 1c), which is presented alongside the corresponding scanning transmission electron microscopy (STEM) high-angle annular dark-field (HAADF) micrograph. These STEM and TEM images of Figure 1c indicate a recombination layer thickness of ~50 nm (nc-Si:H(p<sup>+</sup>) ~25 nm, nc-Si:H(n<sup>+</sup>) ~25 nm).

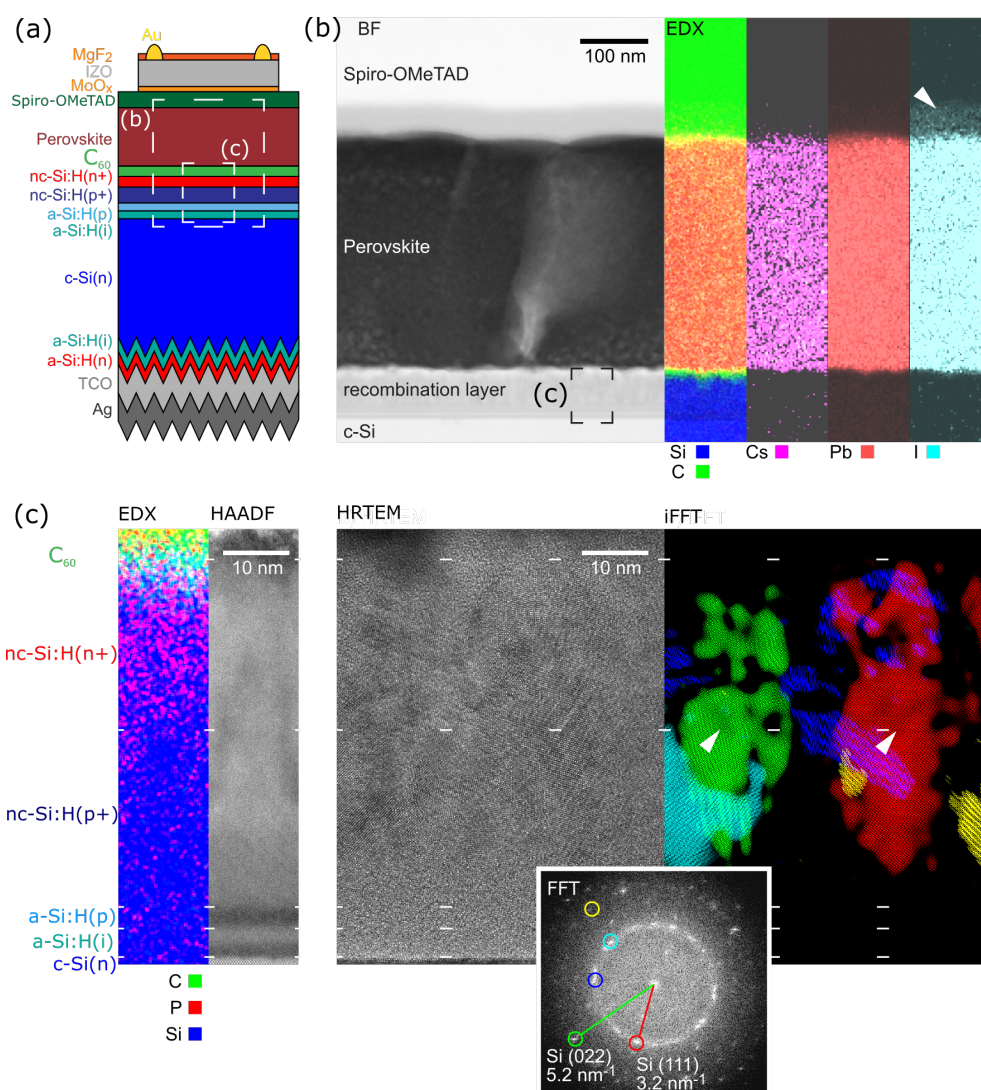


**Figure 1.** a) Schematic view of the perovskite/Si heterojunction tandem cell with a nc-Si:H recombination junction; b) STEM bright-field image of a cross-section of the perovskite cell and corresponding EDX maps of Si K, C K, Cs K, Pb L, I K edges, either combined in the same image or, for the inorganic perovskite elements, shown individually after background subtraction; c) EDX map and corresponding STEM HAADF image of the recombination junction, which show the position of the different interfaces, HRTEM micrograph of the recombination junction, corresponding FFT and superposition of colored inverse FFTs computed from selected Si (111) and (022) reflections (pseudo dark-field image).

The n-i-p perovskite top cell was deposited directly onto the nc-Si:H recombination junction, with a C<sub>60</sub> electron transport layer, a perovskite absorber layer fabricated with a low-temperature two-step deposition method, and a Li-doped spiro-OMeTAD hole transport layer. The perovskite absorber layer was realized by first co-evaporating PbI<sub>2</sub> and CsI with a molar ratio controlled via the respective deposition rates. Then, an organohalide solution containing

either methylammonium (MA) iodide or a mixture of formamidinium (FA) iodide and formamidinium bromide was spin-coated onto the  $\text{PbI}_2\text{:CsI}$  precursor layer, followed by thermal annealing to promote interdiffusion and to obtain either  $\text{Cs}_x\text{MA}_{1-x}\text{PbI}_3$  or  $\text{Cs}_x\text{FA}_{1-x}\text{PbI}_{(1-y)\text{Br}_y}$ . The tandem cells were completed by an  $\text{MoO}_x$ /indium zinc oxide (IZO) transparent front electrode, Au fingers to contact the cells, and an  $\text{MgF}_2$  anti-reflective layer.

To gain more information on the incorporation of cesium into the perovskite layer, energy-dispersive X-ray spectroscopy (EDX) of a  $\text{CsMAPbI}_3$  layer was performed in combination with STEM (Figure 1b). The background-subtracted maps of the Cs  $K\alpha$ , Pb  $L\alpha$  and I  $K\alpha$  edges suggest a uniform distribution of these elements within the perovskite layer (Figure 1b) and a Cs:Pb atomic concentration ratio of  $0.18 \pm 0.03$ , which is consistent with the targeted composition of 0.19 inferred from the CsI:PbI<sub>2</sub> co-evaporation ratio. It should be mentioned that some iodide diffused into the hole transport layer during the processing as already previously observed (marked by an arrowhead in Figure 1b.<sup>[35]</sup> The X-ray diffraction (XRD) pattern presented in the Supplementary Information section confirms the formation of a pure perovskite phase without the peak arising from unreacted  $\text{PbI}_2$  (**Figure S2**).

The monolithic tandem solar cells with the nc-Si:H recombination junction and a  $\text{Cs}_{0.19}\text{MA}_{0.81}\text{PbI}_3$  perovskite top cell reached an efficiency of up to 22.7% on an area of  $0.25 \text{ cm}^2$  and 21.7% on a larger scale of  $1.43 \text{ cm}^2$ , as obtained from  $J$ - $V$  measurements, and steady-state efficiencies of 22.0% and 21.2% during maximum power-point tracking for 1000 s, respectively (**Figure 2a,b**). Moreover, the  $J$ - $V$  curves exhibited negligible hysteresis. These tandem cells showed a high open-circuit voltage ( $V_{oc}$ ) of  $> 1750 \text{ mV}$ , which demonstrates the capability of the nc-Si:H junction to efficiently recombine electrons from the top cell with holes from the bottom cell. The fill factor values are comparable to the ones obtained with a TCO recombination layer reported earlier.<sup>[11]</sup> This suggests that the presence of the nc-Si:H stack does not introduce significant electrical losses.<sup>[33]</sup> In comparison, a rear-side-textured single-junction SHJ solar cell reference for the bottom cell, comprising the nc-

Si:H layer stack at the front, shows an efficiency of 16.45% with a  $V_{oc}$  of 693 mV for an aperture area of  $0.25 \text{ cm}^2$  (Figure S3).

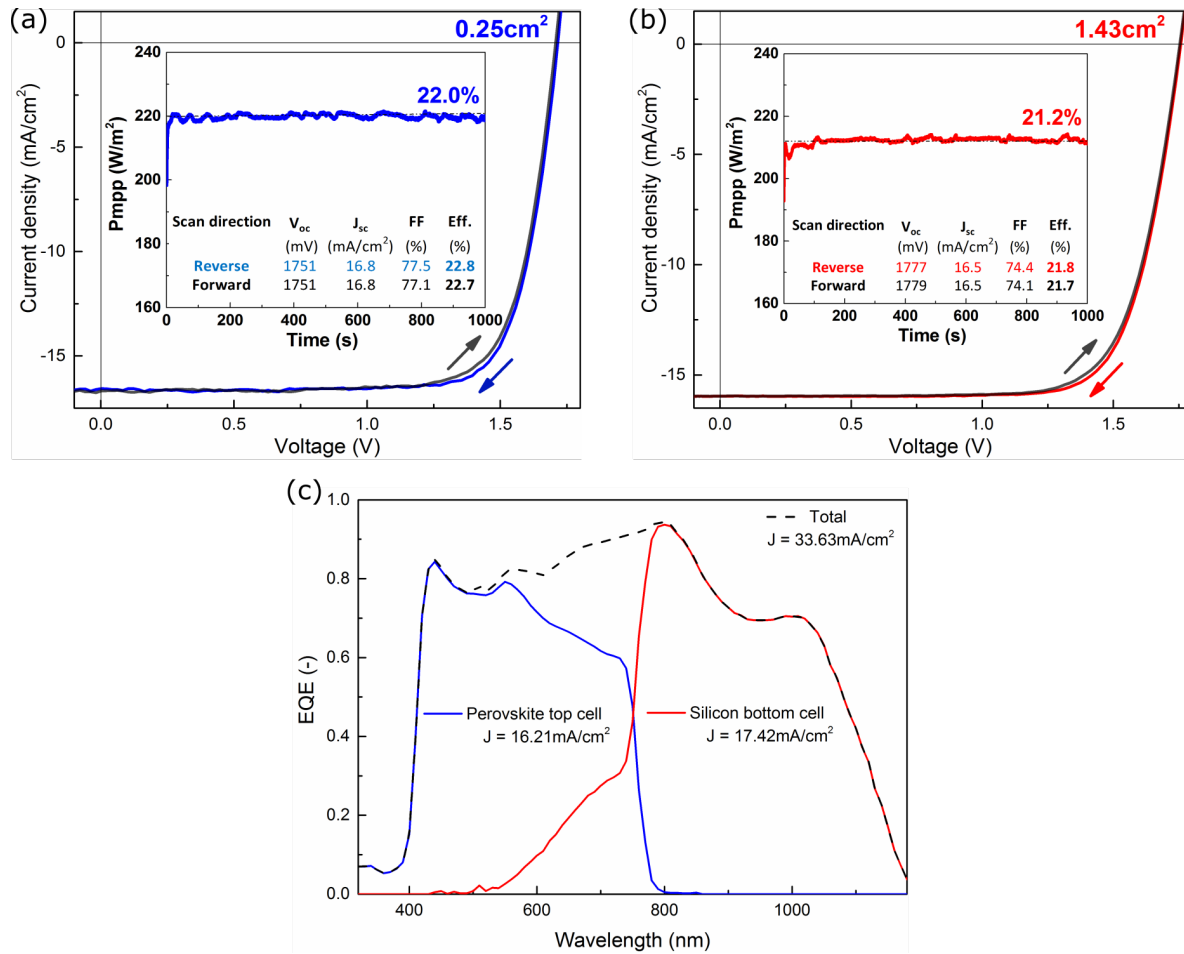


**Figure 2.** a)  $J$ - $V$  curves of perovskite/Si:H monolithic tandem cells (perovskite composition:  $\text{Cs}_{0.19}\text{MA}_{0.81}\text{PbI}_3$ ) with a)  $0.25 \text{ cm}^2$  and b)  $1.43 \text{ cm}^2$  aperture area. c) EQE spectra of the  $0.25 \text{ cm}^2$  tandem cell.

The external quantum efficiency (EQE) spectra of these tandem cells demonstrated a current mismatch of more than  $1 \text{ mA/cm}^2$  between the sub-cells (Figure 2c), with the tandem cell photocurrent being limited by the top cell. In an ideal monolithic tandem device with a c-Si bottom cell, the top cell bandgap should be  $\sim 1.75 \text{ eV}$  to reach current matching.<sup>[36][37]</sup> Here, the  $\text{Cs}_{0.19}\text{MA}_{0.81}\text{PbI}_3$  perovskite bandgap is  $1.58 \text{ eV}$ , well below that optimal value. One main limitation of the top cell current is linked to parasitic absorption in the spiro-OMeTAD layer, which can be avoided by adopting an inverted p-i-n perovskite configuration.<sup>[10]</sup> Considering a gain of  $2 \text{ mA/cm}^2$  in the top cell due to avoiding parasitic absorption in the spiro-OMeTAD

layer and using a perovskite absorber with a bandgap of 1.63 eV (**Figure 6b**), a tandem cell current density of 18.5 mA/cm<sup>2</sup> could be reached. As a result, perovskite/SHJ monolithic tandems with efficiencies of 25% are within reach ( $V_{oc} = 1758$  mV,  $FF = 77\%$ ,  $J_{sc}$  18.5 mA/cm<sup>2</sup>,  $\eta = 25.04\%$ ). As recently demonstrated for the case of interdigitated back-contacted SHJ cells,<sup>[33]</sup> the nc-Si:H recombination layer polarity can be inverted to form an a-Si:H(i)/a-Si:H(n)/nc-Si:H(n+)/nc-Si:H(p+) stack without losing its functionality, hence making this concept compatible with either polarity.

To demonstrate the versatility of the nc-Si:H junction, tandem devices with a top cell based on a Cs<sub>0.19</sub>FA<sub>0.81</sub>Pb(I<sub>0.78</sub>Br<sub>0.22</sub>)<sub>3</sub> perovskite material were fabricated by the sequential deposition protocol described above. XRD diffraction measurements confirmed the presence of the perovskite phase (Figure S2). This absorber has the advantage of being more moisture- and temperature-stable when compared to MA-based perovskite materials.<sup>[38][39]</sup> The chosen Cs<sub>0.19</sub>FA<sub>0.81</sub>Pb(I<sub>0.78</sub>Br<sub>0.22</sub>)<sub>3</sub> composition has a bandgap of 1.63 eV, which can be readily tuned to higher values by increasing the Br content.<sup>[40]</sup> With this absorber and the nc-Si:H recombination layer, a monolithic tandem efficiency of 20.5% is obtained with an aperture area of 0.25 cm<sup>2</sup> (**Figure S4**).

Next, we compared the optical performance of the nc-Si:H junction to an ITO recombination layer. The bandgap of nc-Si:H is considerably smaller than that of ITO, leading to absorption in the blue part of the spectrum (**Figure 3a**). This absorption has, however, only a very limited effect on the tandem cell performance, as the top perovskite cell absorbs all the light up to wavelengths of ~550 nm. In the near-infrared region (> 800 nm), the silicon recombination junction absorbs less light than its ITO counterpart, thus more photons are available to the bottom cell. To assess the effect of the presence of a TCO between both sub-cells, tandem cells with Cs<sub>0.19</sub>FA<sub>0.81</sub>Pb(I<sub>0.78</sub>Br<sub>0.22</sub>)<sub>3</sub> perovskite top cell and nc-Si:H recombination junctions were fabricated, either with or without an additional 40-nm-thick ITO layer sputtered onto the nc-Si:H junction (ITO properties are given in Table S1).

The reflectance spectra of these tandem cells, presented in Figure 3b, show that the reflectance peak at wavelengths of 700-900 nm observed for the tandem without the TCO layer is almost completely suppressed ( $< 2.5\%$ ). In addition, without the intermediate TCO layer, the reflectance is also strongly reduced at wavelengths  $> 1000$  nm. These results can be explained by the fact that nc-Si:H and c-Si have nearly identical refractive indices ( $n_{c-Si} = 3.6-3.7$  at 800 nm), as compared to the considerably lower value of ITO ( $n_{ITO} = 1.6-2$  at 800 nm, depending on its doping).<sup>[41][42]</sup> As a result of the better index matching, the nc-Si:H recombination junction mitigates reflection at the sub-cell interface and thus increases the light transmittance to the SHJ bottom cell.

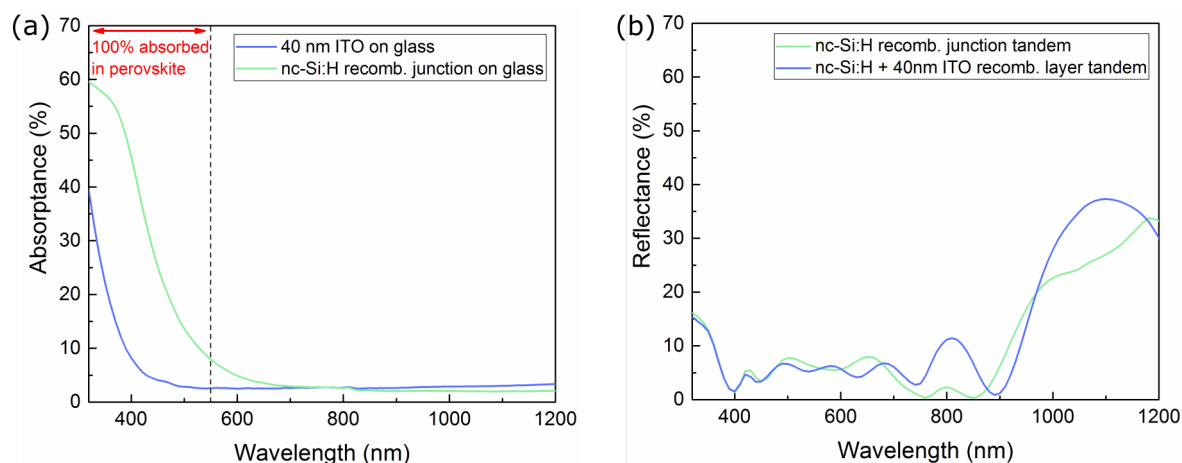


**Figure 3.** a) Absorbance of a 40-nm-thick ITO layer and the nc-Si:H recombination junction deposited on glass; b) Reflectance of monolithic  $C_{0.19}FA_{0.81}Pb(I_{0.78}Br_{0.22})_3/SHJ$  tandem cells with the nc-Si:H junction, either with or without an additional 40-nm-thick ITO layer deposited on it.

EQE spectra shown in Figure 4 confirm these observations and demonstrate the impact of the TCO interlayer on the current distribution between the sub-cells. The EQE of the SHJ bottom cell is considerably higher at wavelengths of 750-950 nm without ITO layer, resulting in an increase in current by more than  $1 \text{ mA/cm}^2$ . In contrast, the current generated in the perovskite top cell is virtually unaffected by the presence of the ITO layer. It is noteworthy that the shape of the bottom cell EQE spectrum strongly depends on the exact thickness of all

layers present in the tandem device, hence the exact current gain in the bottom cell varies.<sup>[11]</sup> Nevertheless, the current gain of  $> 1 \text{ cm}^2$  was reproducible, also with other TCOs (**Figure S5**). These results confirm that using an nc-Si:H recombination junction can significantly improve the optical performance of monolithic tandems using front-side-polished silicon bottom cells.

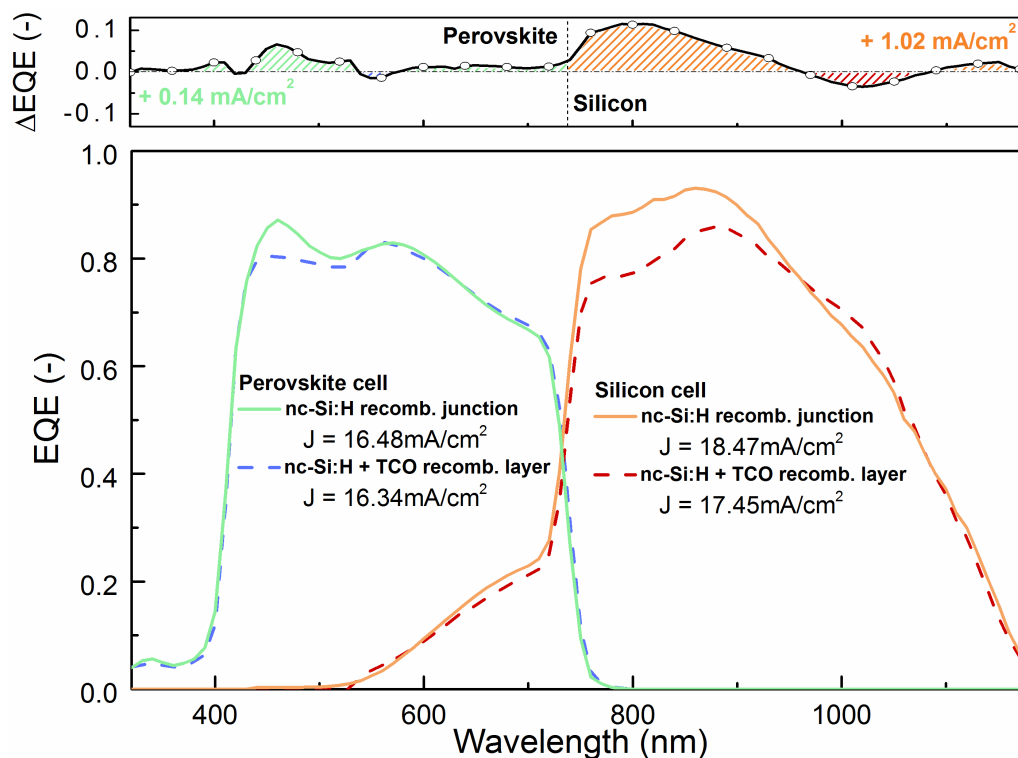


**Figure 4.** EQE spectra of  $C_{0.19}FA_{0.81}Pb(I_{0.78}Br_{0.22})_3/SHJ$  solar cells with a nc-Si:H recombination junction, either with or without an additional 40-nm-thick ITO layer deposited on it.

In addition to the optical advantages, the nc-Si:H recombination junction features a highly anisotropic film conductivity, providing sufficient vertical conductivity while exhibiting low lateral conductivity.<sup>[33]</sup> In monolithic tandem cells, this low lateral conductivity is beneficial, as it reduces possible shunt paths through pinholes or defects present in the perovskite top cell.<sup>[24][43]</sup>  $J$ - $V$  measurements at several light intensities of the perovskite/SHJ tandems with and without a TCO intermediate layer support this hypothesis (see **Figure 5 and S6**). At one sun, both cells show a high  $V_{oc}$ . However, under reduced light intensity, the presence of the ITO layer with high lateral conductivity leads to strong losses in  $V_{oc}$ , indicating an increased

contribution of shunts, whereas the tandem cell without ITO retains a high  $V_{oc}$  even at low illumination.

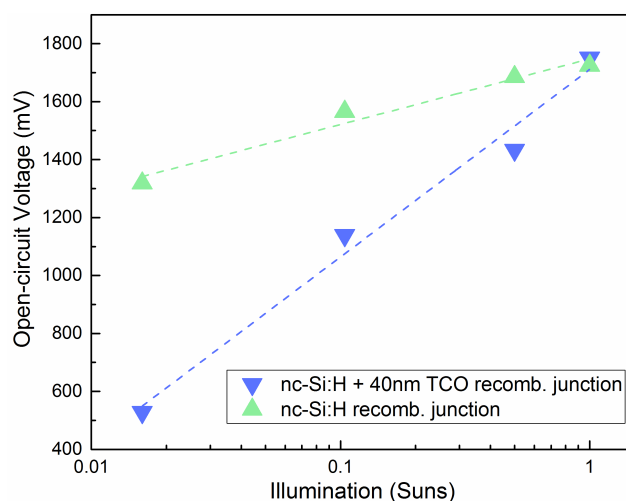


**Figure 5.**  $V_{oc}$  of  $0.25\text{ cm}^2$   $C_{0.19}FA_{0.81}Pb(I_{0.78}Br_{0.22})_3$ /SHJ monolithic tandem cells with nc-Si:H recombination junction, measured at several illumination intensities. Results from cells with and without an additional 40-nm-thick ITO interlayer on top of the nc-Si:H junction are shown.

The high shunt resistance induced by the nc-Si:H recombination junction is an essential ingredient to enable efficient large-area perovskite/SHJ monolithic tandems. To demonstrate the up-scalability of the tandem cells presented here, a  $CS_{0.19}FA_{0.81}Pb(Br_{0.22}I_{0.78})_3$  perovskite top cell was deposited on a  $5\times 5\text{ cm}^2$  SHJ bottom cell with nc-Si:H junction. With an aperture area of  $12.96\text{ cm}^2$ , an efficiency of 18% during maximum power-point tracking is obtained (Figure 6a).

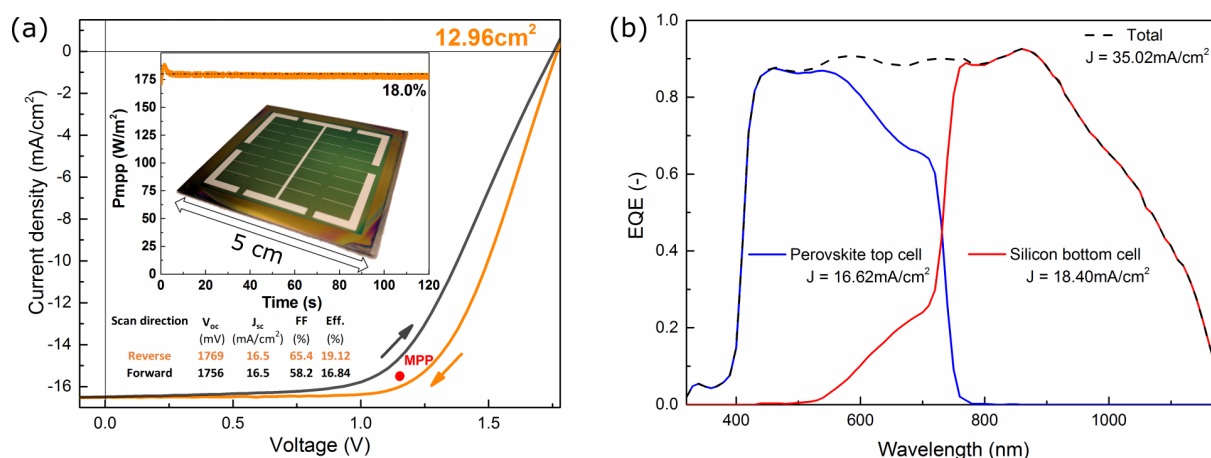


**Figure 6.** 12.96 cm<sup>2</sup> large Cs<sub>0.19</sub>FA<sub>0.81</sub>Pb(Br<sub>0.22</sub>I<sub>0.78</sub>)<sub>3</sub>/SHJ monolithic tandem: a) *J-V* curve and b) corresponding EQE spectra. The inset to a) shows the steady-state power output after 120 s maximum power point tracking and a photo of a finished device on a 5×5 cm<sup>2</sup> substrate.

The discrepancy in efficiency between the large-area devices (12.96 cm<sup>2</sup>) and the smaller ones is significant. However, closer inspection shows that most of the loss in efficiency stems from the lower fill factor. A large part of this loss is caused by the increased series resistance from the top electrode metallization, which consists of 130 nm-thick evaporated Ag fingers. The development of screen-printed Ag metallization as used for commercial silicon solar cells, which readily enables the deposition of sufficiently thick metal electrodes, is expected to greatly reduce this efficiency gap between small and large cells. The *J-V* curve of the larger monolithic tandem shows the presence of hysteresis, which was not observed on the 0.25 cm<sup>2</sup> aperture area devices (see Figure S4). The origin of this hysteresis for the larger cells is still not well understood and is currently under investigation.

### 3. Conclusions

We developed monolithic perovskite/SHJ tandem cells with an nc-Si:H recombination junction deposited by PECVD at low temperatures (< 200°C), reaching steady-state efficiencies of up to 22.0% and 21.2% for aperture areas of 0.25 cm<sup>2</sup> and 1.43 cm<sup>2</sup>, respectively. The presented nc-Si:H junction is fully compatible with the well-established SHJ bottom cell fabrication process, since it can be deposited in the same PECVD reactor as the passivating amorphous layers. Parasitic absorption and reflection losses at the interface between the sub-cells were reduced, increasing the bottom cell current density by more than 1 mA/cm<sup>2</sup> in comparison to a tandem cell containing a TCO recombination layer, yet without compromising the electrical properties of the device. In addition, the low lateral conductivity of the nc-Si:H recombination junction mitigated shunt paths through the perovskite top cell, enabling the demonstration of a 12.96 cm<sup>2</sup> monolithic perovskite/SHJ tandem cell with 18%

steady-state efficiency. Therefore, this work paves the way to high-efficiency large-area perovskite/silicon tandem solar cells.

#### 4. Experimental Section

##### *Monolithic tandem fabrication:*

SHJ bottom cells were fabricated using n-type-doped double-side mechanically polished silicon float-zone wafers with a resistivity of 1-5  $\Omega$  and a thickness of 280  $\mu\text{m}$ . A dielectric etch mask was deposited on one side of the wafer by PEVCD. Single-side texturization was realized by wafer immersion in a KOH-based solution, followed by dielectric mask removal with a diluted HF solution.

Intrinsic and doped hydrogenated amorphous silicon layers were deposited on both sides of the wafer in a PECVD reactor to passivate the silicon surface and to create carrier-selective contacts. The SHJ bottom cell was made in the front-emitter configuration, with the n-type contact at the back and the p-type at the front. The back contact consisted of a sputtered TCO/Ag stack. The p<sup>+</sup>/n<sup>+</sup> nc-Si:H recombination junction was deposited in the same PECVD reactor at low temperatures (< 200°C) onto the p-type amorphous silicon layer at the front side of the SHJ bottom cell. Trimethylboron and phosphine gases were added to the silane/hydrogen mixture in order to form the p- and the n-doped layers.

The perovskite top cell was deposited directly onto the nc-Si:H recombination junction. First, ~8 nm of C<sub>60</sub> (> 99.95%, NanoC) were thermally evaporated to form the electron transport layer in a Lesker Mini-Spectros system, with a substrate temperature of 30°C and a base pressure of < 1.5 × 10<sup>-6</sup> Torr. Then, PbI<sub>2</sub> (> 99.99%, Alfa Aesar) and CsI (> 99%, Abcr) were co-evaporated (165 nm for Cs<sub>x</sub>MA<sub>1-x</sub>PbI<sub>3</sub> and 180 nm for Cs<sub>x</sub>FA<sub>1-x</sub>PbI<sub>(1-y)Br<sub>y</sub></sub>), where the CsI evaporation rate was fixed to 15% of the PbI<sub>2</sub> rate, corresponding to an atomic Cs:Pb ratio of 0.19. The PbI<sub>2</sub>:CsI layer was transformed to the final perovskite phase by spin coating a solution of methylammonium iodide (0.346M, Dyesol) or a mixture of formamidinium bromide:iodide (2:1 molar ratio, 0.445M, Dyesol) in isopropanol at 3000 rpm for 30 s using

dynamic solution dispensing in an inert atmosphere, followed by an annealing step ( $\text{Cs}_y\text{MA}_{1-y}\text{PbI}_3$ : 120°C, 30 min in glovebox,  $\text{Cs}_y\text{FA}_{1-y}\text{PbI}_{3-x}\text{Br}_x$ : 150°C, 30 min in ambient air). A spiro-OMeTAD solution in chlorobenzene (72.3 mg/mL 2,2',7,7'-tetrakis(N,N-di-4-methoxyphenylamino)-9,9'-spirobifluorene (> 99.5%, Lumtec), 28.8  $\mu\text{L}/\text{ml}$  4-tert-butylpyridine (> 96.0%, TCI), and 17.5  $\mu\text{L}/\text{ml}$  stock solution of 520 mg/mL lithium bistrifluoromethylsulfonyl imide (> 97.0%, Sigma-Aldrich) in acetonitrile was then spin coated at 4000 rpm for 30 s.

The transparent electrode consisted of a 20-nm-thick  $\text{MoO}_x$  (> 99.98%, Sigma Aldrich) buffer layer deposited by thermal evaporation at a rate of 0.5  $\text{\AA}/\text{s}$  and 100 nm of sputtered indium zinc oxide (from a 90%  $\text{In}_2\text{O}_3$  + 10% ZnO target) with a resistivity of  $\sim 55 \Omega/\square$ .<sup>[44]</sup> Au (130 nm) or Ag (130 nm, for  $5 \times 5 \text{ cm}^2$  tandems) were thermally evaporated through a shadow mask to form the metallic contact. For the large-area tandem cells, the metal fingers shaded about 3.8% of the total aperture area. Finally, an antireflective coating ( $\sim 100 \text{ nm}$  of  $\text{MgF}_2$  (> 99.99%, Umicore)) was deposited onto the cells by thermal evaporation.

#### *Device characterization:*

We used a UV-VIS-NIR spectrophotometer (PerkinElmer Lambda 900) with an integrating sphere to acquire total reflectance, transmittance, and absorbance spectra. Current density-voltage ( $J$ - $V$ ) measurements were performed using a two-lamp (halogen and xenon) class AAA WACOM sun simulator with an AM1.5G irradiance spectrum at  $1000 \text{ W}/\text{m}^2$ . Shadow masks were used to define the illuminated area. The monolithic tandem cells were measured with a scan rate of 100 mV/s. Maximum power point tracking was realized through an in-house-written LabVIEW code.<sup>[11]</sup> External quantum efficiency (EQE) spectra were obtained on a custom-made spectral response set-up with a lock-in amplifier, using chopped light at a frequency of 232 Hz. For tandem cells, blue and red light biases were used to saturate the complementary sub-cell. Furthermore, a voltage bias of 0.7 V and 1.1 V was applied to measure the sub-cells in short-circuit conditions (0.7 V for the perovskite and 1.1 V for the

silicon cell). The microstructure of the tandem cells was investigated using high-resolution transmission electron microscopy performed in an image and probe Cs-corrected FEI Titan Themis microscope operated at 200 kV. STEM BF and HAADF images were combined to EDX to assess the chemistry of the different layers. EDX fitting was performed using the Cliff-Lorimer method.<sup>[45]</sup> Images and chemical maps were acquired using a convergence semi-angle of 28 mrad and a beam current of either 400 pA (at lower magnification) or 200 pA (at higher magnification). FFTs of high-resolution TEM micrographs and iFFTs of selected Si (111) and (022) reflections were computed with a mask diameter of 0.6 1/nm using an in-house-written Mathematica script. For each individual iFFT, the contrast, brightness and gamma values were adjusted manually to highlight the Si crystallites. TEM samples were prepared using the conventional focused ion beam (FIB) lift-off technique, which was performed in a Zeiss Nvision 40 FIB/scanning electron microscope workstation. A final thinning voltage of 2 kV was used to reduce gallium-induced implantation and amorphisation damage. The TEM samples were quickly transferred in air (< 2 min) from the vacuum of the FIB/SEM to the TEM to reduce any degradation of the perovskite.<sup>[35]</sup> XRD measurements were carried out in an Empyrean diffractometer (Panalytical) equipped with a PIXcel-1D detector. The diffraction patterns were measured using a Cu K $\alpha$  radiation (wavelength of 1.54 Å). Raman spectroscopy was performed on a-Si:H(i)/a-Si:H(p)/nc-Si:H(p+)/nc-Si:H(n+) stacks deposited on glass. To obtain the crystallinity, the data was fitted and deconvolved using Lorentzians. The crystallinity was defined as the ratio between the area below the curve of the crystalline peaks (at 510 cm<sup>-1</sup> and 519 cm<sup>-1</sup>) over the sum of the crystalline and amorphous peaks.

**Supporting Information ((delete if not applicable))**

Supporting Information is available from the Wiley Online Library or from the author.

## 5. Acknowledgements

The authors acknowledge Fabien Debrot and Christophe Allebé for SHJ wet chemical processing and Vincent Paratte for Raman spectroscopy measurement. This work was funded by the Nano-Tera.ch “Synergy” project, the Swiss Federal Office of Energy under Grant SI/501072-01, and the Swiss National Science Foundation via the NRP70 “Energy Turnaround” project “PV2050”.

Received: ((will be filled in by the editorial staff))

Revised: ((will be filled in by the editorial staff))

Published online: ((will be filled in by the editorial staff))

## References

- [1] Fraunhofer ISE, *Agora Energiewende* **2015**, 82.

- [2] M. A. Green, *Nat. Energy* **2016**, *1*, 1.
- [3] M. Saliba, T. Matsui, J.-Y. Seo, K. Domanski, J.-P. Correa-Baena, N. Mohammad K., S. M. Zakeeruddin, W. Tress, A. Abate, A. Hagfeldt, M. Grätzel, *Energy Environ. Sci.* **2016**, *9*.
- [4] E. H. Anaraki, A. Kermanpur, L. Steier, K. Domanski, T. Matsui, W. Tress, M. Saliba, A. Abate, M. Grätzel, A. Hagfeldt, J.-P. Correa-Baena, *Energy Environ. Sci.* **2016**, *9*, 3128.
- [5] S. De Wolf, J. Holovsky, S. J. Moon, P. Löper, B. Niesen, M. Ledinsky, F. J. Haug, J. H. Yum, C. Ballif, *J. Phys. Chem. Lett.* **2014**, *5*, 1035.
- [6] G. E. Eperon, S. D. Stranks, C. Menelaou, M. B. Johnston, L. M. Herz, H. J. Snaith, *Energy Environ. Sci.* **2014**, *7*, 982.
- [7] P. Löper, S.-J. Moon, S. M. de Nicolas, B. Niesen, M. Ledinsky, S. Nicolay, J. Bailat, J.-H. Yum, S. De Wolf, C. Ballif, *Phys. Chem. Chem. Phys.* **2014**, 1619.
- [8] N. N. Lal, T. P. White, K. R. Catchpole, *IEEE J. Photovoltaics* **2014**, *4*, 1380.
- [9] S. Albrecht, M. Saliba, J. P. Correa Baena, F. Lang, L. Kegelmann, M. Mews, L. Steier, A. Abate, J. Rappich, L. Korte, R. Schlatmann, M. K. Nazeeruddin, A. Hagfeldt, M. Grätzel, B. Rech, J. Rg Rappich, L. Korte, R. Schlatmann, M. K. Nazeeruddin, A. Hagfeldt, M. Grätzel D, B. Rech, M. Grätzel, B. Rech, *Energy Environ. Sci.* **2016**, *9*, 81.
- [10] K. A. Bush, A. F. Palmstrom, Z. (Jason) Yu, M. Boccard, R. Cheacharoen, J. P. Mailoa, D. P. McMeekin, R. L. Z. Hoyer, C. D. Bailie, T. Leijtens, I. M. Peters, M. C. Minichetti, N. Rolston, R. Prasanna, S. E. Sofia, D. Harwood, W. Ma, F. Moghadam, H. J. Snaith, T. Buonassisi, Z. C. Holman, S. F. Bent, M. D. McGehee, *Nat. Energy* **2017**, *17009*, 1.
- [11] J. Werner, C.-H. H. Weng, A. Walter, L. Fesquet, J. P. Seif, S. De Wolf, B. Niesen, C. Ballif, *J. Phys. Chem. Lett.* **2016**, *7*, 161.

- [12] F. Fu, T. Feurer, T. P. Weiss, S. Pisoni, E. Avancini, C. Andres, S. Buecheler, A. N. Tiwari, *Nat. Energy* **2016**, *2*, 16190.
- [13] G. E. Eperon, T. Leijtens, K. A. Bush, R. Prasanna, T. Green, J. T.-W. Wang, D. P. McMeekin, G. Volonakis, R. L. Milot, R. May, A. Palmstrom, D. J. Slotcavage, R. A. Belisle, J. B. Patel, E. S. Parrott, R. J. Sutton, W. Ma, F. Moghadam, B. Conings, A. Babayigit, H.-G. Boyen, S. Bent, F. Giustino, L. M. Herz, M. B. Johnston, M. D. McGehee, H. J. Snaith, *Science*. **2016**, *354*, 861.
- [14] M. Taguchi, A. Yano, S. Tohoda, K. Matsuyama, Y. Nakamura, T. Nishiwaki, K. Fujita, E. Maruyama, *IEEE J. Photovoltaics* **2014**, *4*, 96.
- [15] Z. C. Holman, A. Descoedres, S. De Wolf, C. Ballif, *IEEE J. Photovoltaics* **2013**, *3*, 1243.
- [16] K. Yoshikawa, H. Kawasaki, W. Yoshida, T. Irie, K. Konishi, K. Nakano, T. Uto, D. Adachi, M. Kanematsu, H. Uzu, K. Yamamoto, *Nat. Energy* **2017**, *2*, 17032.
- [17] J. Werner, L. Barraud, A. Walter, M. Bräuninger, F. Sahli, D. Sacchetto, N. Tétreault, B. Paviet-Salomon, S.-J. Moon, C. Allebé, M. Despeisse, S. Nicolay, S. De Wolf, B. Niesen, C. Ballif, *ACS Energy Lett.* **2016**, *1*, 474.
- [18] T. Duong, Y. Wu, H. Shen, J. Peng, X. Fu, D. Jacobs, E. Wang, T. C. Kho, K. C. Fong, M. Stocks, E. Franklin, A. Blakers, N. Zin, K. McIntosh, W. Li, Y. Cheng, T. P. White, K. Weber, K. Catchpole, *Adv. Energy Mater.* **2017**, *1700228*, 1.
- [19] H. Uzu, M. Ichikawa, M. Hino, K. Nakano, T. Meguro, J. L. Hernández, H. S. Kim, N. G. Park, K. Yamamoto, *Appl. Phys. Lett.* **2015**, *106*, DOI 10.1063/1.4905177.
- [20] T. Todorov, T. Gershon, O. Gunawan, C. Sturdevant, S. Guha, *Appl. Phys. Lett.* **2014**, *105*, 2012.
- [21] J. Werner, A. Walter, E. Rucavado, S.-J. J. Moon, D. Sacchetto, M. Rienaecker, R. Peibst, R. Brendel, X. Niquille, S. De Wolf, P. Löper, M. Morales-Masis, S. Nicolay, B. Niesen, C. Ballif, S. De Wolf, P. Löper, M. Morales-Masis, S. Nicolay, B. Niesen, C.

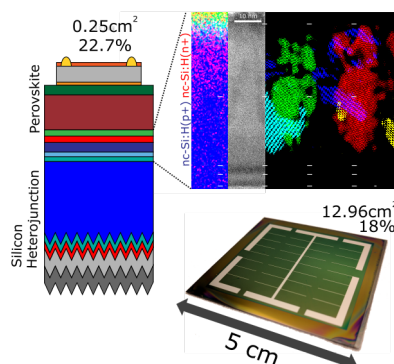
- Ballif, *Appl. Phys. Lett.* **2016**, *109*, 2.
- [22] Z. C. Holman, A. Descoedres, L. Barraud, F. Z. Fernandez, J. P. Seif, S. De Wolf, C. Ballif, *IEEE J. Photovoltaics* **2012**, *2*, 7.
- [23] D. T. Grant, K. R. Catchpole, K. J. Weber, T. P. White, *Opt. Express* **2016**, *24*, DOI 10.1364/OE.24.0A1454.
- [24] P. Buehlmann, J. Bailat, D. Domiń, A. Billet, F. Meillaud, A. Feltrin, C. Ballif, *Appl. Phys. Lett.* **2007**, *91*, DOI 10.1063/1.2794423.
- [25] M. Despeisse, G. Bugnon, A. Feltrin, M. Stueckelberger, P. Cuony, F. Meillaud, A. Billet, C. Ballif, *Appl. Phys. Lett.* **2010**, *96*, DOI 10.1063/1.3324704.
- [26] C. Amano, H. Sugiura, A. Yamamoto, M. Yamaguchi, *Appl. Phys. Lett.* **1987**, *51*, 1998.
- [27] J. Meier, S. Dubail, R. Fluckiger, D. Fischer, H. Keppner, A. Shah, *Proc. 1994 IEEE 1st World Conf. Photovolt. Energy Convers. - WCPEC (A Jt. Conf. PVSC, PVSEC PSEC)* **1994**, *1*, 409.
- [28] G. J. Bauhuis, P. Mulder, J. J. Schermer, *Prog. Photovoltaics Res. Appl.* **2014**, *22*, 656.
- [29] J. P. Mailoa, C. D. Bailie, E. C. Johlin, E. T. Hoke, A. J. Akey, W. H. Nguyen, M. D. McGehee, T. Buonassisi, *Appl. Phys. Lett.* **2015**, *106*, DOI 10.1063/1.4914179.
- [30] H. Keppner, P. Torres, J. Meier, R. Platz, D. Fischer, U. Kroll, S. Dubail, J. A. Anna Selvan, N. Pellaton Vaucher, Y. Ziegler, R. Tschanner, C. Hof, N. Beck, M. Goetz, P. Pernet, M. Goerlitzer, N. Wyrsh, J. Veuille, J. Cuperus, A. Shah, J. Pohl, *MRS Proc.* **1996**, *452*, 865.
- [31] P. Alpuim, V. Chu, J. P. Conde, *J. Vac. Sci. Technol. A* **2001**, *19*, 2328.
- [32] G. Nogay, J. P. Seif, Y. Riesen, A. Tomasi, Q. Jeangros, N. Wyrsh, F. J. Haug, S. De Wolf, C. Ballif, *IEEE J. Photovoltaics* **2016**, *6*, 1654.
- [33] A. Tomasi, B. Paviet-Salomon, Q. Jeangros, J. Haschke, G. Christmann, L. Barraud, A. Descoedres, J. P. Seif, S. Nicolay, M. Despeisse, S. De Wolf, C. Ballif, *Nat. Energy* **2017**, *2*, 17062.

- [34] J. P. Seif, A. Descoeurdes, G. Nogay, S. Hanni, S. M. De Nicolas, N. Holm, J. Geissbuhler, A. Hessler-Wyser, M. Duchamp, R. E. Dunin-Borkowski, M. Ledinsky, S. De Wolf, C. Ballif, *IEEE J. Photovoltaics* **2016**, *6*, 1132.
- [35] Q. Jeangros, M. Duchamp, J. Werner, M. Kruth, R. E. Dunin-Borkowski, B. Niesen, C. Ballif, A. Hessler-Wyser, *Nano Lett.* **2016**, *16*, 7013.
- [36] A. Shah, P. Torres, R. Tscharnner, N. Wyrsh, H. Keppner, *Science*. **1999**, *285*, 692.
- [37] I. Almansouri, A. Ho-Baillie, S. P. Bremner, M. A. Green, *IEEE J. Photovoltaics* **2015**, *5*, 968.
- [38] F. C. Hanusch, E. Wiesenmayer, E. Mankel, A. Binek, P. Angloher, C. Fraunhofer, N. Giesbrecht, J. M. Feckl, W. Jaegermann, D. Johrendt, T. Bein, P. Docampo, *J. Phys. Chem. Lett.* **2014**, *5*.
- [39] T. Leijtens, K. A. Bush, R. Cheacharoen, R. Beal, A. R. Bowring, M. D. McGehee, *J. Mater. Chem. A* **2017**, *0*, 1.
- [40] D. P. McMeekin, G. Sadoughi, W. Rehman, G. E. Eperon, M. Saliba, M. T. Horantner, A. Haghighirad, N. Sakai, L. Korte, B. Rech, M. B. Johnston, L. M. Herz, H. J. Snaith, *Science*. **2016**, *351*, 151.
- [41] H. Kim, C. M. Gilmore, A. Piqué, J. S. Horwitz, H. Mattoussi, H. Murata, Z. H. Kafafi, D. B. Chrisey, *J. Appl. Phys.* **1999**, *86*, 6451.
- [42] Z. C. Holman, M. Filipič, A. Descoeurdes, S. De Wolf, F. Smole, M. Topič, C. Ballif, *J. Appl. Phys.* **2013**, *113*, DOI 10.1063/1.4772975.
- [43] Z. Song, J. Werner, N. Shrestha, F. Sahli, S. De Wolf, B. Niesen, S. C. Watthage, A. B. Phillips, C. Ballif, R. J. Ellingson, M. J. Heben, *J. Phys. Chem. Lett.* **2016**, *7*, 5114.
- [44] J. Werner, G. Dubuis, A. Walter, P. Löper, S. J. Moon, S. Nicolay, M. Morales-Masis, S. De Wolf, B. Niesen, C. Ballif, *Sol. Energy Mater. Sol. Cells* **2015**, DOI 10.1016/j.solmat.2015.06.024.
- [45] G. Cliff, G. W. Lorimer, *J. Microsc.* **1975**, *103*, 203.

**The table of contents entry should be 50–60 words long**, and the first phrase should be bold.

The entry should be written in the present tense and impersonal style. The text should be different from the abstract text.

A **nanocrystalline silicon recombination junction** is presented, which mitigates reflection losses in monolithic perovskite/silicon heterojunction tandem solar cells, resulting in efficiencies of up to 22.7% on 0.25 cm<sup>2</sup> aperture area. Thanks to its low transversal conductance, this recombination junction enables tandem cell up-scaling, leading to steady-state efficiencies of 18% on 12.96 cm<sup>2</sup> aperture area.



ToC figure ((Please choose one size: 55 mm broad × 50 mm high **or** 110 mm broad × 20 mm high. Please do not use any other dimensions))

((Supporting Information can be included here using this template))

Copyright WILEY-VCH Verlag GmbH & Co. KGaA, 69469 Weinheim, Germany, 2016.

## Supporting Information

### Improved Optics in Monolithic Perovskite/Silicon Tandem Solar Cells with a Nanocrystalline Silicon Recombination Junction

Florent Sahli, Brett A. Kamino, Jérémie Werner, Matthias Bräuninger, Bertrand Paviet-Salomon, Loris Barraud, Raphaël Monnard, Johannes Peter Seif, Andrea Tomasi, Quentin Jeangros, Aïcha Hessler-Wyser, Stefaan De Wolf, Matthieu Despeisse, Sylvain Nicolay, Bjoern Niesen, and Christophe Ballif

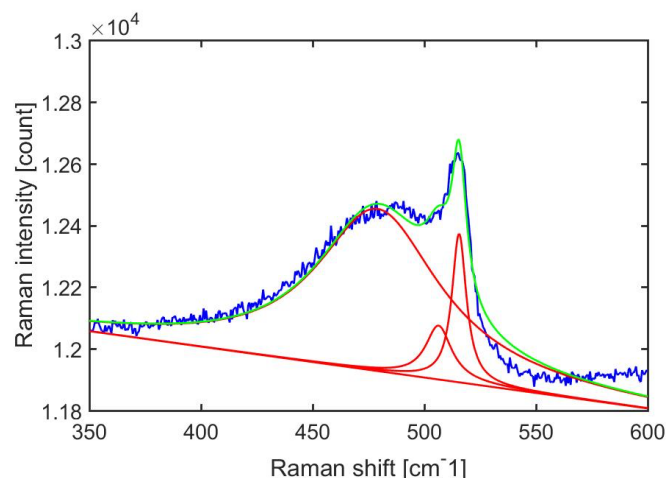


**Figure S1.** Raman spectrum of a nanocrystalline silicon p-n recombination junction deposited on a glass substrate (glass/a-Si:H(i)/a-Si:H(p)/nc-Si:H(p+)/nc-Si:H(n+)). The crystallinity fraction of the full amorphous/nanocrystalline stack was extracted by deconvoluting the Raman shift by three Lorentzian curves centered at  $480\text{ cm}^{-1}$  for the amorphous peak, at  $519\text{ cm}^{-1}$  for the crystalline peak, and a third curve at  $510\text{ cm}^{-1}$ . The crystallinity fraction is defined as the ratio between the area below the curve of the crystalline peaks (at  $510\text{ cm}^{-1}$  and  $519\text{ cm}^{-1}$ ) over the total area below the crystalline and amorphous peaks.

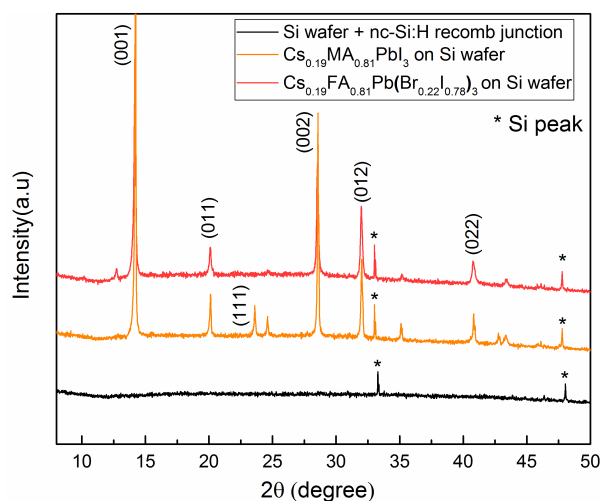


**Figure S2.** X-ray diffractograms of the perovskite absorber materials used in this study, as well as of a silicon wafer reference. The perovskite layers were deposited onto SHJ bottom cells, coated with the nc-Si:H recombination junction and the  $C_{60}$  electron transport layer to provide a substrate for perovskite growth identical to that in fully processed tandem cells. In the  $Cs_{0.19}FA_{0.81}Pb(Br_{0.22}I_{0.78})_3$  diffractogram, a low-intensity peak appears at  $12.7^\circ$   $2\theta$ , which is due to the presence of unconverted  $PbI_2$ .

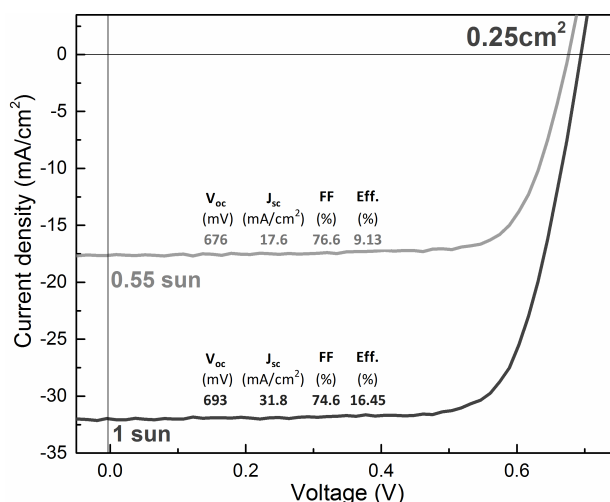


**Figure S3.** *J-V* curve of a rear-side-textured SHJ solar cell at different illumination intensities with a 100-nm-thick transparent IZO front electrode and a thermally evaporated Ag contact. The aperture area is 0.25 cm<sup>2</sup>.

	Thickness (nm)	Carrier conc. (cm <sup>-3</sup> )	Res. (Ωcm)	mobility (cm <sup>2</sup> /Vs)	Sheet res. (Ω/sq)
Indium tin oxide	40	2.17·10 <sup>20</sup>	5.88·10 <sup>-4</sup>	48	146

**Table S1.** Electrical properties of the indium tin oxide (ITO) recombination layer.

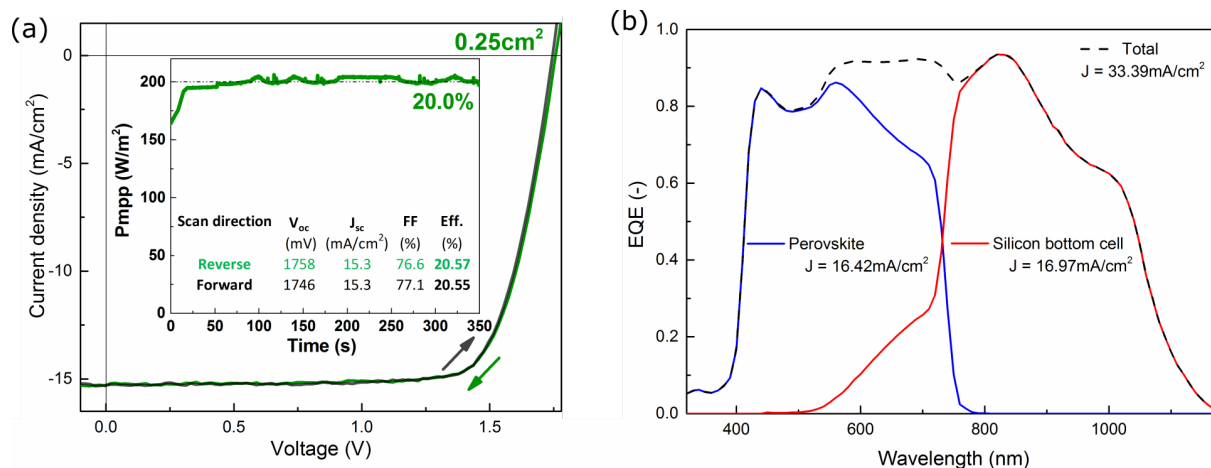


**Figure S4.** a) *J-V* curve of a Cs<sub>0.19</sub>FA<sub>0.81</sub>Pb(Br<sub>0.22</sub>I<sub>0.78</sub>)<sub>3</sub> perovskite/SHJ monolithic tandem with nc-Si:H recombination junction on a double-side-polished wafer, with an aperture area of 0.25 cm<sup>2</sup>. b) Corresponding external quantum efficiency (EQE) spectra.

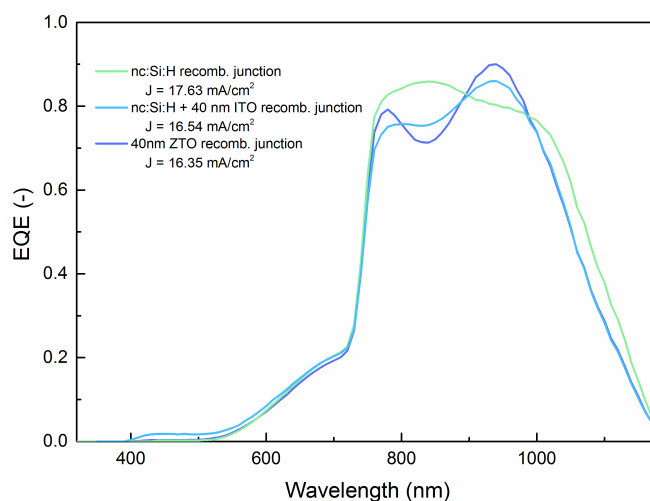


**Figure 5.** EQE spectra of SHJ bottom cells of  $0.25 \text{ cm}^2$   $\text{Cs}_{0.19}\text{FA}_{0.81}\text{Pb}(\text{Br}_{0.22}\text{I}_{0.78})_3$  perovskite/SHJ monolithic tandems on double-side-polished wafers with either a nc-Si:H, nc-Si:H + 40 nm ITO, or 40 nm ZTO recombination junction.

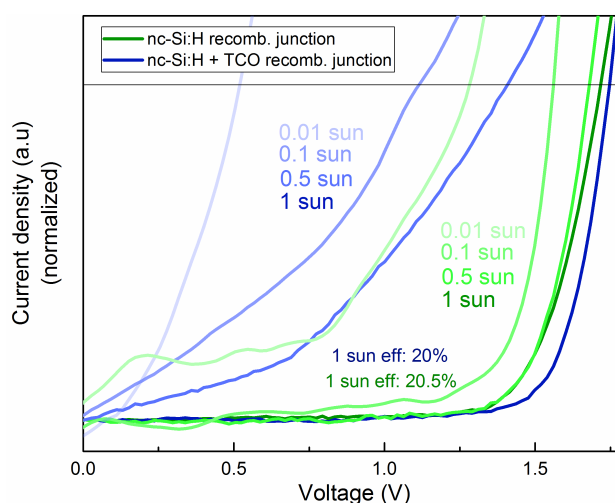


**Figure S6.** Normalized  $J$ - $V$  curves measured at several light intensities (1, 0.5, 0.104 and 0.016 suns) of  $\text{Cs}_{0.19}\text{FA}_{0.81}\text{Pb}(\text{Br}_{0.22}\text{I}_{0.78})_3$  perovskite/SHJ monolithic tandem cells with nc-Si:H recombination junction, with and without an additional 40-nm-thick ITO layer deposited on the recombination junction to assess the influence of the presence of an intermediate layer with high lateral conductivity. The aperture area was  $0.25 \text{ cm}^2$ .